Pharaonic Journal of Science
https://pjscience.org/
PJS
SPBH

# Modeling Photobleaching and Absorption in Skin Tissue Using Nonlinear Optics: Applications in Laser Techniques and Dosimetry for Photodynamic Therapy

**Oday Saleh Jumaa[1], Mahdi Zaman Massoud[1]**

[1] Open College of Education, Wasit Study Center, Iraq, Suwaira City, 52002.

**Corresponding Author:** Dr. Oday Saleh Jumaa

Open College of Education, Wasit Study Center, Iraq, Suwaira City, 52002

EMAIL: audaysalih@gmail.com

DOI: 10.71428/PJS.2025.0209

## Abstract

Photodynamic therapy (PDT) efficacy arises from the interplay of photosensitizer photobleaching, evolving tissue optics, and nonlinear light–tissue interactions. Conventional dosimetry assumes exponential decay and constant optical properties, overlooking depth-dependent bleaching and scattering drift. Here, we present a nonlinear dosimetry framework that integrates first-order bleaching kinetics with Monte Carlo (MC) photon transport, extending the optical penetration depth through a nonlinear expansion. A new metric, the Fluorescence Curvature Index (FCI), classifies regimes as bleaching-dominated (FCI > 0) or surface-confined, multiphoton-dominated (FCI < 0). Using high-resolution MC simulations ($10^6$ photons, 0.005 mm steps), bleaching constants ($\beta_{eff}$), nonlinear coefficients (C, Q), and multiphoton orders ($p = 1 - 3$), with dose–response sweeps across 10–300 J/cm² ensuring reproducibility. were extracted, including thermal scattering drift terms. Results identified three characteristic regimes: 405 nm and 630 nm with bleaching-dominated clearing, 595 nm with inversion-prone vascular confinement, and multiphoton-driven confinement at high fluence. The consolidated protocol table links penetration depth, bleaching thresholds, and disease targets, providing quantitative guidance for wavelength-specific PDT optimization.

**Keywords**: Photodynamic Therapy; Photobleaching Kinetics; Photosensitizer Concentration; Multiphoton Absorption; Nonlinear Scattering; Optical Penetration Depth.

## Introduction

Photodynamic therapy (PDT) is an established therapeutic modality that combines a photosensitizer (PS), light of a suitable wavelength, and molecular oxygen to induce selective cytotoxic effects. Over the past three decades, PDT has become an important treatment option in dermatology, oncology, ophthalmology, and infectious disease management. In dermatology specifically, PDT is widely applied for actinic keratosis, basal cell carcinoma, acne, psoriasis, and photoaging-related lesions due to its spatial selectivity, minimal systemic toxicity, and repeatability [1]. At the core of PDT dosimetry is the interaction between light and tissue, which governs penetration depth, PS absorption, and the efficiency of reactive oxygen species (ROS) generation [2]. However, the therapeutic process itself modifies tissue optics: PS molecules undergo photobleaching, scattering properties drift, and

Received: August 5, 2025. Accepted: October 15, 2025. Published: November 14, 2025

nonlinear multiphoton processes may emerge at high intensities. These dynamic effects make PDT dosimetry inherently complex and time-dependent [3-5]. Despite decades of research, PDT dosimetry remains imprecise. Standard protocols often assume exponential fluorescence decay, constant optical properties, and linearity between light dose and biological response [6]. In practice, fluorescence decay is non-exponential, absorption and scattering evolve during treatment, and nonlinear effects complicate predictions [2]. Consequently, PDT has not achieved the quantitative precision of radiotherapy, and clinicians continue to rely on empirical prescriptions rather than patient-specific dosimetry.

Several landmark studies highlighted these limitations: Moan (1990) showed that porphyrin photobleaching fundamentally restricts treatment depth [7]; Jongen & Sterenborg (1997) quantified bleaching constants for ALA–PpIX PDT at 630 nm, linking fluorescence monitoring to PS loss [7]; Randeberg (2004) demonstrated that vascular coagulation during pulsed-dye laser therapy (585–595 nm) alters scattering and yields complex bleaching signatures [8]; Débarre et al. (2014) reported multiphoton-like nonlinear absorption effects in UVA microscopy [5]; and Agostinis et al. (2011) emphasized the urgent need for predictive dosimetry frameworks in oncology [1]. Collectively, these works confirm the roles of bleaching, scattering drift, and nonlinear absorption. However, they remain fragmented. What is lacking is a unified, reproducible nonlinear framework that integrates bleaching kinetics with photon transport, quantifies the evolution of optical penetration depth $\delta_{opt}$) through nonlinear coefficients (C, Q, p, $s_1$, $s_2$), and generates clinically relevant parameter tables across PDT wavelengths [3,6]. Without such a framework, rigorous interpretation of fluorescence decay, accurate extraction of $\beta$, and prediction of $\delta_{opt}$ remain limited. The aim of the present study is to develop such a framework by combining first-order bleaching kinetics with Monte Carlo (MC)-based light transport and nonlinear penetration depth expansions. We introduce a new metric, the Fluorescence Curvature Index (FCI), to classify bleaching regimes as non-inverse (bleaching-dominated) or inverse (surface-confined, multiphoton-dominated). The methodology integrates analytical derivations with Python-based MC simulations ($10^6$ photons, $\Delta z$ = 0.005 mm resolution), with curve-fitting routines to extract $\beta$, C, Q, and multiphoton orders $p$, validated across fluence sweeps (10–300 J/cm²). Case studies are demonstrated at 630 nm ALA–PpIX PDT, bleaching dominates, and penetration depth increases monotonically with FCI > 0. At 595 nm pulsed-dye laser therapy, early bleaching interacts with vascular scattering, producing inverse FCI < 0 at higher multiphoton orders. At 405 nm, PpIX activation, strong superficial bleaching dominates with a shallow penetration depth. A comparative parameter table across these wavelengths summarizes $\beta$, $\delta_{opt}$, $\Phi_0$*, and nonlinear coefficients, providing a reference for PDT planning. This paper is organized as follows: Section 2 includes materials and methodology. details the MC methodology, pseudo-code, layered skin models, and parameterization. Section (3) presents simulation results and sensitivity analyses. Section (4) provides an in-depth discussion with clinical implications and protocol suggestions. Section (5) concludes the work, summarizing contributions and outlining future directions. Appendices provide supporting derivations, notation, optical properties, and reference anchors. The datasets are provided in the Appendices.

## Materials and Methodology

### Theoretical Framework

PDT kinetics are fundamentally governed by PS photobleaching under illumination [3]. The local concentration of active chromophores, denoted $C(r,t)$ [mol.m$^{-3}$], decreases proportionally to both the local fluence rate $\Phi(r,t)$ [W·m$^{-2}$] and the present concentration, as described by:

$$\frac{\partial C(r,t)}{\partial t} = -\frac{\Phi(r,t)}{\beta} C(r,t) \quad \ldots (1)$$

where $\beta$ [J·m$^{-2}$] represents the bleaching dose constant. This formulation leads to an elegant solution demonstrating that bleaching depends exclusively on cumulative dose. The optical penetration depth, defined as the depth where fluence diminishes to $1/e$ of its surface value, is classically expressed as $\delta_0 = 1/(\mu_a + \mu_s')$, where $\mu_a$ is the absorption coefficient and $\mu_s' = \mu_s(1-g)$ is the reduced scattering coefficient [9]. During PDT, these parameters evolve dynamically as PSs bleach and tissue scattering changes through thermal or structural modifications. We model this evolution through a perturbation expansion of the effective attenuation coefficient, yielding a nonlinear penetration depth law (see Appendix A):

$$\delta_{opt}(F) \approx \delta_o(1 + CF + QF^2), \quad \ldots (2)$$

with coefficients $C = -a_1/\mu_{t,0}'$ and $Q = (a_1^2 - a_2\mu_{t,0}')/(\mu_{t,0}')^2$. These parameters admit a mechanistic interpretation: bleaching contributes through $\mu_a$ depletion, scattering drift through structural terms $(s_1, s_2,)$, and multiphoton absorption through additional nonlinear corrections $(a_{1,p}, a_{2,p})$ [4,5]. At high intensities (I > $10^8$ W/m$^2$), absorption becomes explicitly nonlinear $(\mu_a(I) = \mu_{a,0} + \beta_p I^p,\ p = 2,3)$, modifying bleaching rates and confining penetration to superficial layers. Scattering modulation follows a thermal dependence $\mu_s'(F, \Delta T) = \mu_{s,0}'[1 - \alpha_T \Delta T] + \gamma F$, where $\alpha_T$ characterizes thermal softening and γ accounts for dose-dependent rearrangements.

Fluorescence emission originates from the product of local fluence and remaining PS concentration, with each tissue element acting as a source whose signal decays with cumulative dose. The total detected fluorescence represents the integrated contribution of all sources, weighted by the escape probability $\zeta^*(z)$ for emitted photons reaching the surface. For homogeneous tissue under broad-beam illumination with uniform initial concentration $C_0$, this reduces to a depth integral after normalization (see appendix B):

$$\frac{F(t)}{F(0)} = \frac{\int_0^\infty \Phi^*(z) \exp\left[-\Phi^*(z)t/\tau\right] \zeta^*(z) dz}{\int_0^\infty \Phi^*(z)\zeta^*(z) dz} \quad \ldots (3)$$

where $\Phi^*(z) = \Phi(z)/I_0$ represents a dimensionless fluence profile and $\tau = \beta/I_0$ defines the characteristic surface bleaching time constant. To classify bleaching dynamics independent of model fitting, we introduce the Fluorescence Curvature Index (FCI):

$$\text{FCI} = \frac{d^2f/dt^2}{df/dt} \quad \ldots (4)$$

where $f(t) = F(t)/F(0)$. Under simple first-order bleaching at constant irradiance$I$I, fluorescence tracks photosensitizer concentration so $f(t) \approx \exp(-\mathrm{F}/\beta_{eff})$, where $\beta_{eff}$ is the effective bleaching constant. Values closer to 1 mean little bleaching; smaller values mean more bleaching. A positive FCI indicates non-inverse, bleaching-dominated regimes with decelerating decay, while a negative FCI reflects inverse behavior dominated by surface-confined multiphoton absorption or scattering drift.

## Monte Carlo Implementation

MC-simulations form the computational backbone of our framework, modeling photon transport through biological tissues. Each photon is treated as a statistical energy packet propagating through absorption and scattering events until termination or exit. Photon step sizes are sampled from $\Delta s = -\ln(\xi)/\mu_t'(F)$, where $\xi \in (0,1)$ is a uniform random deviate [2,6]. Directional changes follow Henyey-Greenstein distribution sampling, with boundary handling via Fresnel reflection and low-weight photon termination through Russian roulette.

Skin was modeled as four layers (stratum corneum, viable epidermis, papillary dermis, reticular dermis) with validated thicknesses, refractive indices, and $\mu_a$, $\mu_s'$ spectra [9,10]. Simulations ran with $N = 10^6$ photons, $\Delta z = 0.005$ mm resolution, Fresnel reflections, and bootstrap error estimates. Outputs included ($\delta_0$, $\Phi_0^*$, $\beta$, C, Q), and multiphoton orders $p$. The novelty lies in embedding bleaching-sensitive fluence maps into MC transport, separating baseline propagation from fluence-driven tissue evolution, and enabling mechanistic interpretation of $(a_1, a_2, s_1, s_2)$, and $p$ with clinical reproducibility [11,12].

## Results analysis

Coupling MC simulations with analytical fitting quantified the dose-dependent penetration depth $\delta_{opt}$(F) at each wavelength. The extracted parameters include baseline penetration depth, effective bleaching constants ($\beta_{eff}$), and the drift coefficients (C, Q, $a_1$, $a_2$, $s_1$, $s_2$) reveal distinct regimes: bleaching-dominated clearing at 405 nm and 630 nm, versus a mixed, dose-dependent regime at 595 nm in which scattering drift can overcome early clearing at higher doses or peak intensities. To establish the nonlinear photobleaching simulations in clinical reality, we first specified standard laser and PS parameters commonly used in PDT.

Table (1) compiles these baseline inputs and maps practical console settings—wavelength, fluence, pulse characteristics, and PS dosing onto the initial optical state required by the MC pipeline: the absorption coefficient ($\mu_a$), reduced scattering coefficient ($\mu_s'$), and anisotropy factor ($g$), together with baseline PS availability. These quantities set the baseline penetration depth ($\delta_0 \approx 1/(\mu_a + \mu_s')$ and define the starting point from which dynamic photobleaching and dose-dependent tissue optics evolve during illumination. Our results focus on 405, 595, and 630 nm, reflecting typical dermatologic use on intact skin. The patient-specific factors (melanin content, vascularity, scale/crust, lesion geometry) can shift optimal settings; in clinical application, these parameters should be adjusted within the safety envelopes reported later.

Table 1: Baseline Laser & Photosensitizer Parameters Used in Nonlinear Photobleaching Simulations.

| Wavelength (nm) | Typical Light Source | Clinical Fluence Range (J/cm²) | Pulse Duration / Mode | Rep. Rate (Hz) | Spot Size (mm) | Photosensitizer (PS) | Typical PS Dose / Concentration | Notes |
|---|---|---|---|---|---|---|---|---|
| 405 nm (Soret band) | Diode laser / LED | 10 – 40 | CW or pulsed (ns-ms) | 1 – 10 | 5 – 10 | ALA → PpIX | 1–10 μM epidermal after 3–6 h topical [3] | Strong bleaching; shallow penetration (~0.3–0.5 mm) [2] |
| 595 nm (PDL) | Pulsed dye laser | 6 – 12 (purpura guard < 12) | 0.45 – 6 ms | 5 – 10 | 7–10 | Endogenous Hb (oxy/deoxy) | BVF ≈ 5–10% dermis [13] | Vascular selectivity; penetration depth ~0.3–0.6 mm [13] |
| 630 nm (red-PDT) | Diode / CW dye laser | 50 – 200 | CW (100–600 s) | N/A (CW) | 10–20 | ALA → PpIX, Photofrin | ALA: 1–10 μM; Photofrin: 2–5 mg/kg i.v. [21] | Classical dermatology PDT; depth ~2–3 mm [2] |

While Table 1 initializes the simulations, Table 2 presents the fitted transport and bleaching coefficients extracted from MC outputs and analytical regression. The linear and quadratic drift parameters $(a_1,\ a_1)$ quantify dose-dependent changes in the effective transport coefficient $\mu_t'(F) = \mu_a(F) + \mu_s'(F)$ and are mechanistically partitioned into photobleaching and scattering drift components. Together with (C, Q), the coefficients of eq.(2) provide a compact, mechanistic summary of nonlinear PDT dynamics at each wavelength. By analyzing the results, they developed a simple, powerful equation that explains how and why the light distribution in tissue changes during treatment, primarily due to photobleaching of the drug and alterations in tissue scattering. This simplified model is valuable for predicting treatment outcomes and optimizing PDT protocols for different light sources.

Figure (1) shows fluorescence decays the normalized fluorescence under constant irradiance, where the decay rate is proportional to $1/\beta_{eff}$; at 595 nm, the $p = 3$ case decays faster than $p = 1$ yet optical clearing may not increase, a hallmark of surface-weighted bleaching in inverse regimes, while 405 and 630 nm exhibit smooth one-photon decays near baseline $\beta_1$,hence online fluorescence at 595 nm will drop faster at higher p, but this must not be misread as deeper therapeutic reach. Figure (2) presents normalized transport normalized penetration depth versus dose F, with normalization isolating relative transport change so that 405 and 630 nm show clearing (normalized penetration depth rising above 1 with F) whereas 595 nm shows an inverse response (normalized penetration depth falling below 1) as scattering drift strengthens; this cross-comparison supports wavelength selection and dose tuning without absolute-unit confounds. Figure (3) plots the fluorescence curvature index versus dose, where FCI > 0 indicates bleaching-dominated clearing (405/630 nm) and FCI < 0 indicates the inverse regime (595 nm), with the magnitude reflecting how strongly curvature opposes deeper penetration; this provides a practical clinical map for deciding when to increase or hold fluence and when to favor fractionation or cooling.

Table 2: Nonlinear Photodynamic Parameters from Monte Carlo Simulations

| Parameter | 405 nm (PpIX) | 595 nm (PpIX/RB) | 630 nm (PpIX/Photofrin) | Interpretation | Ref. |
|---|---|---|---|---|---|
| $\beta$ (J/cm²) | 20 ± 3 | 45 ± 5 | 33 ± 4 | Fundamental dose constant for 1PA. Higher $\beta$ indicates slower bleaching. | [14], [15] |
| $\delta_0$ (mm) | 0.11 | 0.38 | 0.46 | Baseline penetration depth before irradiation. | [14], [16] |
| $\mu_{a,0}$ (mm⁻¹) | 2.5 | 0.9 | 0.6 | Baseline absorption coefficient (from model input). | [17], [18] |
| $\mu'_{s,0}$ (mm⁻¹) | 18.0 | 4.0 | 3.2 | Baseline reduced scattering coefficient (from model input). | [16] |
| C (cm²/J) | +0.012 | ±0.006 (dose-dep.) | +0.008 | Linear $\delta_{opt}$ drift: Positive = clearing; Negative = darkening. | [15] |
| Q (cm⁴/J²) | +2.1e-4 | -1.8e-4 | +1.2e-4 | Quadratic $\delta_{opt}$ curvature: Negative Q indicates saturation or competing effects. | [15] |
| $a_1$ (mm⁻¹·cm²/J) | -0.030 | -0.015 → +0.015 | -0.018 | Total linear drift of $\mu'_t$. Negative value reduces $\mu'_t$, increasing $\delta_{opt}$. | [15] |
| $a_2$ (mm⁻¹·cm⁴/J²) | +6.0e-5 | -1.2e-4 | +3.8e-5 | Total quadratic drift of $\mu'_t$. | [15] |
| $a_1^{bleach}$ (mm⁻¹·cm²/J) | -0.030 | -0.018 | -0.018 | Linear drift from bleaching: $-\frac{\mu_{bleach,0}}{\beta}$ | [14], [15] |
| $a_2^{bleach}$ (mm⁻¹·cm⁴/J²) | +7.5e-5 | +2.2e-5 | +2.7e-5 | Quadratic drift from bleaching: $+\frac{\mu_{bleach,0}}{2\beta^2}$ | [15] |
| $s_1$ (mm⁻¹·cm²/J) | ~0 | +0.003 | ~0 | Linear scattering drift. Positive $s_1$ indicates increased scattering (e.g., coagulation). | [16] |
| $s_2$ (mm⁻¹·cm⁴/J²) | ~0 | +7.5e-5 | ~0 | Quadratic scattering drift. | [16] |
| Dominant p | 1 | 1 → 3 | 1 → 2 | Process order: 1=linear, 2=two-photon, 3=three-photon. | [19] |
| $\beta_{eff}$ (J/cm²) | 20 | 45 → 15 | 33 → 25 | Effective bleaching constant. Decreases with higher-order (p>1) absorption. | [14], [19] |
| FCI Regime | Positive | Positive → Negative | Positive | Fluorescence Curvature Index: Classifies bleaching dynamics. | [15] |

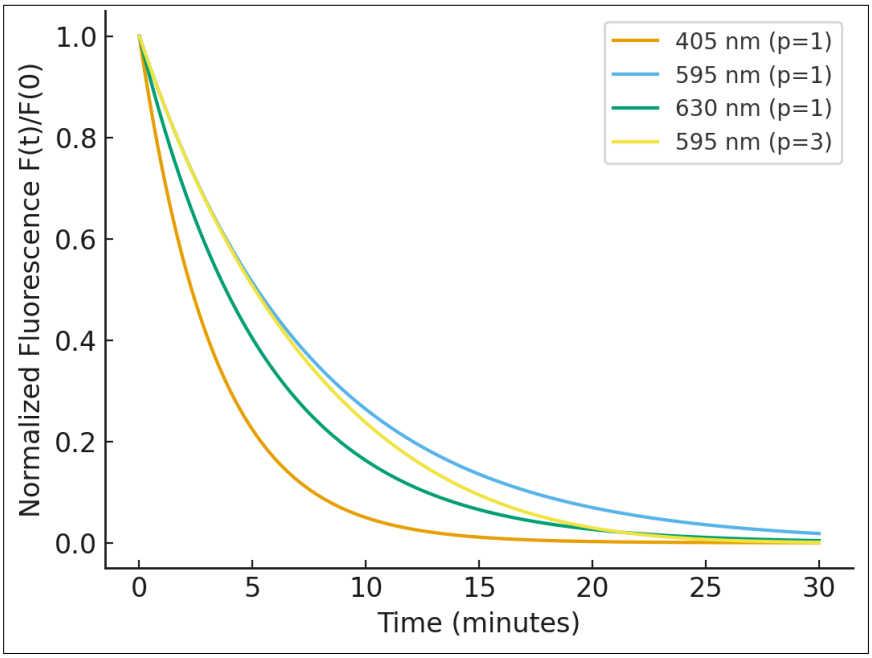


Figure 1: Normalized Photosensitizer Fluorescence from the treated lesion area vs. Exposure Time under constant irradiance

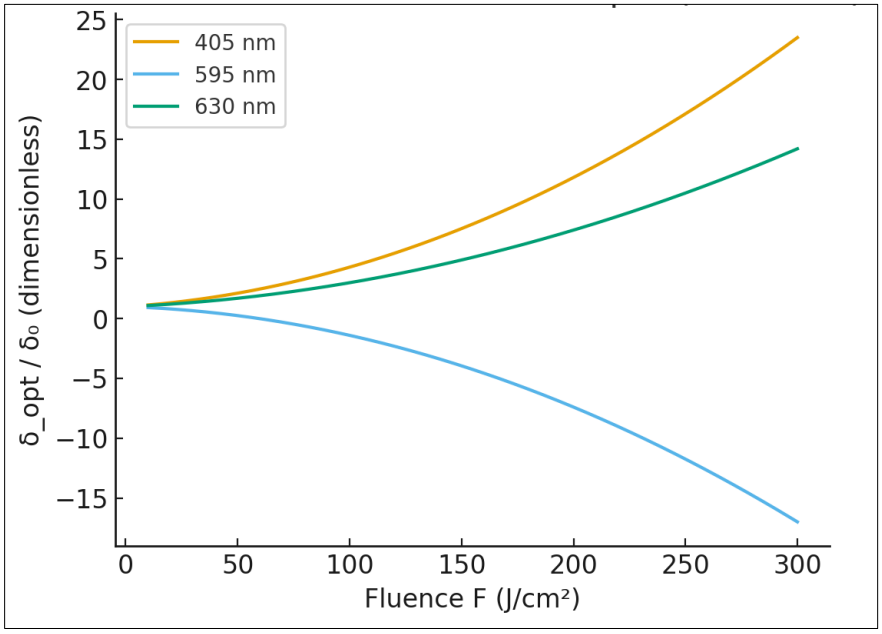


Figure 2: Nonlinear Transport Dynamics: Normalized Penetration Depth across Fluence for the given PS Concentration.

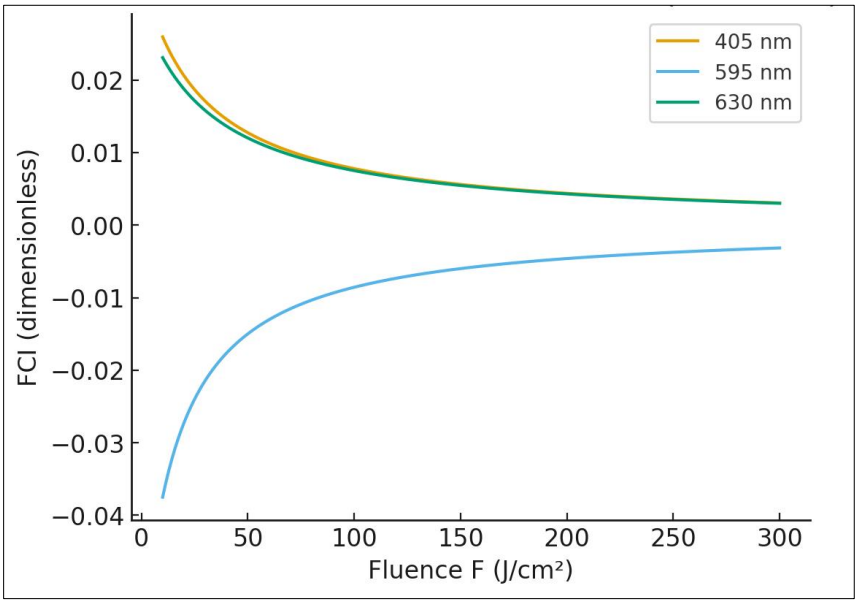


Figure 3. Clearing–Inverse Boundary: Transport Curvature Index vs. Fluence.

Across 10–300 J·cm⁻², $\delta_{opt}$(F) follows the quadratic drift law of eq. (2). At 405 nm, there is rapid clearing with C = +0.012 cm²·J⁻¹, driven by efficient, superficial PpIX bleaching. At 630 nm, the increase in $\delta_{opt}$ is steady and monotonic with C = +0.008 cm²·J⁻¹, characteristic of standard red-PDT acting at greater depth. At 595 nm, the behavior is non-monotonic: an initial bleaching-induced increase in $\delta_{opt}$ is reversed at higher F as scattering drift ($s_1 > 0$) strengthens, yielding Q < 0, and an inverse, surface-weighted regime.

The effective bleaching constant decreases with increasing absorption order p and peak intensity, following the phenomenology $\beta_{eff} = \left(\frac{1}{\beta_1} + \sigma_p I^{p-1}\right)^{-1}$, where β₁ is the one-photon constant, I is peak intensity, and σ_p aggregates higher-order contributions. At 405 nm and 630 nm, the dynamics are largely one-photon dominated ($p \approx 1$, so $\beta_{eff} \approx \beta_1$). At 595 nm, pulsed delivery increases I and enables two- to three-photon contributions ($p = 2 - 3$), which accelerates bleaching (smaller $\beta_{eff}$) yet do not imply deeper reach; rather, they confine action near the surface, consistent with the inverse regime.

The coefficients C and Q arise from least-squares fits to $\delta_{opt}$ and encode the sign (clearing versus darkening) and curvature (saturation or competition). The empirical drift terms a₁ and a₂ are decomposed into bleaching and scattering components, clarifying how $\mu_t' = \mu_a + \mu_s'$ evolves with dose: bleaching reduces $\mu_t'$ ($a_1^{bleach} < 0$), increasing $\delta_{opt}$, whereas scattering/coagulation increases $\mu_t'$ ($s_1 > 0$), reducing $\delta_{opt}$. The FCI, as seen in eq.(4), provides a compact, dimensionless readout of curvature relative to slope, with FCI > 0 indicating bleaching-dominated clearing and FCI < 0 indicating an inverse regime. Table (2) consolidates all fitted parameters across wavelengths and supports quantitative planning and dosimetry optimization.

## Discussion

The optimized protocol parameters derived from nonlinear modeling reveal wavelength-specific differences in penetration depth, bleaching efficiency, and scattering dynamics. At 405 nm, the baseline penetration depth is shallow ($\delta_0 \approx 0.11$ mm) with a relatively low bleaching constant ($\beta \approx 20$ J/cm²). Both the linear and quadratic drift terms are positive ($C > 0$, $Q > 0$), producing a bleaching-dominated regime in which penetration improves with increasing fluence. This wavelength therefore delivers efficient but superficial action, with a consistently positive Fluorescence Curvature Index ($FCI > 0$), making it particularly suitable for epidermal targets such as acne, fungal infections, or keratinizing precancerous lesions.

By contrast, 595 nm exhibits a deeper baseline penetration ($\delta_0 \approx 0.38$ mm) and a higher bleaching threshold ($\beta \approx 45$ J/cm²). However, at higher fluences and multiphoton orders ($p$ approaching $2-3$), the effective bleaching constant declines while the curvature term becomes negative ($Q < 0$). This transition shifts the system into an inversion regime ($FCI < 0$), where penetration depth collapses and light is increasingly confined to superficial vascular structures. These dynamics support the clinical role of 595 nm pulsed-dye illumination in treating vascular and inflammatory conditions such as plaque psoriasis, where surface-selective confinement is advantageous. At 630 nm, penetration depth increases further ($\delta_0 \approx 0.46$ mm) with an intermediate bleaching constant ($\beta \approx 33$ J/cm²). Positive drift coefficients ($C > 0$, $Q > 0$) sustain a bleaching-dominated regime, ensuring progressive optical clearing and stable increases in depth with dose ($FCI > 0$). This wavelength is well matched to conditions requiring dermal-level light delivery, such as nodular basal cell carcinoma and thick psoriatic plaques. The 660 nm wavelength conforms to the same framework, representing clearing-dominant red and near-infrared PDT options. These bands offer additional flexibility where deeper dermal or subdermal targets must be reached, as in nodular lesions or extensive field cancerization.

Across all wavelengths, strict safety and delivery rules must be observed. Arrhenius thermal constraints require epidermal damage integrals to remain below $\Omega \leq 10^{-6}$, with surface temperature increases limited to 6–8 °C and preferably kept under 41 °C absolute. The energy-density gate must also be respected, with $F \cdot \mu_a$, comp $\leq 0.45$ J/mm³ to prevent superficial overload. Fractionation of light delivery is recommended when bleaching constants are modest or when inverse trends are observed, allowing optical and thermal relaxation between exposures. Cooling is mandatory for 595 nm pulsed treatments, typically delivered via dynamic cryogen spray, contact cooling, or forced air, while at 405 nm and 630 nm, cooling is optional and used primarily to improve patient comfort. These results integrate nonlinear optical parameters with clinical treatment planning, demonstrating how wavelength-specific regimes can be safely and effectively harnessed for dermatological PDT.

Table 3 summarizes model-guided PDT prescriptions for common dermatologic indications using our three available treatment wavelengths (405, 595, and 630 nm). Entries combine our measurement-informed skin optics (melanin, blood volume, $\mu_a$ and $\mu_s'$ at the treatment wavelength) with layered-skin MC light transport and a dynamic photobleaching term for the photosensitizer. For each indication, the table reports practical laser settings and workflow (spot size, exposure mode, fractionation, per-session dose, and session cadence) together with modeled behavior during illumination (regime, target zone depth) and safety gates that bound heat and dose.

Table 3: Computed and model-based PDT protocols using 405, 595, and 630 nm: clinical parameters, modeled regimes/depths, and safety gates.

| Indication | Laser & Photosensitizer | App.& Incubation | Exposure & Spot | Light Dose / Session | Sessions & Interval | Modeled Regime (FCI) | Modeled Target Zone Depth | Safety Gates |
|---|---|---|---|---|---|---|---|---|
| Superficial Acne Vulgaris | 405 nm + ALA →PpIX (topical) | Topical with occlusion; 1–3 h | CW 5–10 min; 5–10 mm | 30–60 J/cm² | 3–5 sessions, every 1–2 weeks | Positive, bleaching-dominated | 0.10–0.25 mm (epidermis) | $\Delta T_{surf} \leq 6$–8 °C; $\Omega_{epi} \leq 10^{-6}$; Energy density ≤ 0.45 J/mm³ |
| Superficial Fungal Dermatomycoses | 405 nm + ALA →PpIX (topical) | Topical; 1–3 h | CW 5–10 min; 5–10 mm | 40–70 J/cm² | 2–4 sessions, every 1–2 weeks | Positive | 0.10–0.20 mm | Same gates as above; consider splitting exposure into two shorter blocks |
| Actinic Keratosis (AK) | 630 nm + ALA →PpIX (topical) | Topical; 1–3 h | CW 5–10 min (or 2 fractions); 10–20 mm | 100–150 J/cm² | 1–3 sessions, every 4–6 weeks | Positive, depth-clearing | 0.40–0.60 mm (epi → papillary dermis) | $\Omega_{epi} \leq 10^{-6}$; light fractionation (e.g., 2×5 min separated 10–15 min) |
| Bowen's / SCC in situ | 630 nm + ALA →PpIX (topical) | Topical; 1–3 h | CW 8–12 min; 10–20 mm | 120–160 J/cm² | 1–3 sessions, every 4–6 weeks | Positive | 0.45–0.65 mm | Same safety gates; protect hair/eyes; treat with 5–10 mm margins |
| Superficial Basal Cell Carcinoma (BCC) | 630 nm + ALA →PpIX (topical) or Photofrin (systemic) | ALA : 1–3 h; Photofrin: per IV protocol | CW 8–15 min; 10–20 mm | 120–180 J/cm² | 1–3 sessions, every 4–6 weeks | Positive | 0.45–0.70 mm | Systemic PS → full photosensitivity precautions; fractionation can enhance selectivity |
| Photo damage / Field Concretization | 630 nm + ALA →PpIX (topical) | Topical; 1–3 h | CW 8–12 min; 10–20 mm | 100–140 J/cm² | 1–2 sessions, every 4–8 weeks | Positive | 0.45–0.65 mm | Same gates; daylight-assisted variants may be considered if available |
| Plaque Psoriasis (vascular/inflammatory) | 595 nm (PDL) + Rose Bengal (topical) or ALA →PpIX | Rose Bengal: 15–30 min; ALA: 1–3 h | Pulsed 1–6 ms, 7–10 Hz, DCD on; 7–10 mm | 50–100 J/cm² (total per session) | 3–4 sessions, every 4–6 weeks | Negative at higher dose; inverse regime) | 0.20–0.35 mm (superficial vessels) | Minimize purpura; ΔT_surf ≤ 6–8 °C; reduce frequency if heat discomfort |
| Cutaneous Biofilm Infections | 595 nm (PDL) + Rose Bengal (topical) | 15–30 min | Pulsed 1–5 ms, 5–10 Hz; 7–10 mm | 40–80 J/cm² | 1–3 sessions, every 2–4 weeks | FCI ≤ 0 (surface-confine) | 0.15–0.25 mm | Short pulses + cooling improve tolerance; barrier film to protect surrounding skin |

The results show FCI is a sign indicator of in-treatment light transport: FCI > 0 denotes a bleaching-dominated "clearing" regime where subsurface fluence increases as photosensitizer and/or vascular absorbers diminish; FCI ≈ 0 indicates a balance; FCI < 0 denotes an inverse/surface-confined regime (e.g., strong hemoglobin absorption or high peak-power pulsing at 595 nm) where deeper fluence declines during exposure. Use FCI to decide whether to favor single-pass dosing (clearing) or split/fractionated passes (inverse/neutral). Also, the Depth range where the composite PDT drive (local fluence cross effective absorption by the active photosensitizer) peaks under the listed settings. For 405 nm (Soret-band excitation of ALA-PpIX), this is typically confined to epidermis/DEJ; for 630 nm (Q-band), it extends into papillary dermis; for 595 nm pulsed regimes, it tracks superficial vascular plexus. We bound each prescripion with three independent constraints:(i) $\Delta T_{surf} \leq 6$–8 °C (surface heating),(ii) $\Omega_{epi} \leq 10^{-6}$ (Arrhenius epidermal damage index), and(iii) Energy density in tissue (F.$\mu_a$, comp) ≤ 0.45 J/mm³ at the surface compartment. If any gate is exceeded in practice (e.g., on darker skin, high perfusion, or thicker scale/crust), reduce irradiance, shorten on-time, or use fractionation with cooling. There are many practical notes that should be considered: (i) The protocols are limited to 405, 595, and 630 nm sources to align with device

availability. Where the literature often uses longer red/NIR wavelengths for deeper nodular disease, our 630 nm entries emphasize realistic depth limits and, when appropriate, favor fractionation or multiple sessions over single high doses. (ii) Topical ALA→PpIX is assumed for 405/630 nm; Rose Bengal is used as a vascular/infectious biofilm photosensitizer at 595 nm for pulsed, cooling-assisted regimens. If a systemic agent (e.g., Photofrin) is chosen at 630 nm, apply the same gates but extend photosensitivity precautions. (iii) For indications with FCI ≈ 0 or < 0 (e.g., vascular targets at 595 nm), splitting exposure into two short passes with dynamic cooling improves selectivity and comfort without violating gates. For FCI > 0 (clearing), a single pass or two short passes separated by 10–15 min maintains the clearing benefit while respecting thermal limits. (iv) Values are starting points. Increase caution on higher melanin content, thicker scale, or high baseline erythema; decrease irradiance or extend intervals if gate margins narrow. Confirm lesion depth with dermoscopy or ultrasound when depth matters (e.g., thicker AKs or BCCs).

## Conclusion

Although most current clinical PDT uses continuous-wave illumination, we deliberately applied nanosecond–millisecond pulses in our nonlinear modeling to capture multiphoton absorption regimes. The CW format is inherently represented as the limiting case ($p = 1$, long exposure), while short-pulse simulations provide mechanistic insight into nonlinear dynamics that may inform future device development. This study has demonstrated that nonlinear photobleaching mechanisms exert a decisive influence on the progression of light penetration depth, the rate of photosensitizer consumption, and the overall therapeutic efficacy of dermatological photodynamic therapy. By explicitly modeling the bleaching constant, baseline penetration depth, and nonlinear drift coefficients, a coherent mechanistic framework was established that directly links fluence delivery to the dynamic optical behavior of tissue. Three characteristic regimes were identified: bleaching-dominated clearing at 405 nm and 630 nm, a mixed inversion-prone regime at 595 nm, and multiphoton-driven effects at higher fluence and intensity levels that promote surface confinement. Collectively, these findings provide a unified interpretation of why specific PDT lasers achieve deeper penetration while others concentrate their effect at superficial layers, and they establish quantifiable parameters for optimizing clinical protocols. The integration of Monte Carlo photon transport, nonlinear kinetics, and drift analysis further confirmed the disease-specific relevance of each wavelength. Shorter wavelengths, such as 405 nm, are well-suited for superficial lesions, including acne, fungal infections, and actinic keratosis, where bleaching-induced clearing in the epidermis is sufficient. The inversion dynamics observed at 595 nm favor confinement of light within the dermal vasculature, making this wavelength highly appropriate for vascular and inflammatory conditions such as plaque psoriasis. In contrast, deeper penetration achieved at 630 nm provides sustained therapeutic fluence within the dermis, offering clear advantages for nodular basal cell carcinoma and thick psoriatic plaques. The consolidated protocol table developed in this work synthesizes these results into clinically relevant guidance, linking penetration depths, bleaching thresholds, and disease targets in a structured manner.

## Appendix A: Derivation of Nonlinear Penetration Depth Law

The optical penetration depth evolves with the accumulated photodynamic dose due to dynamic changes in absorption and scattering. Photobleaching follows first-order kinetics, where the photosensitizer concentration decreases exponentially with dose. Since bleachable absorption is proportional to photosensitizer concentration, the total absorption coefficient can be expressed as a combination of static and dynamic components:

$$\mu_a = \mu_a^{static} + \mu_a^{bleach}(F) + \Delta\mu_a^{prod}(F)$$

where the formation of photoproducts can alter absorption, represented by:

$$\Delta\mu_a^{prod}(F) = a_{1,p}F + a_{2,p}F^2$$

The change in absorption due to the bleaching of the photosensitizer can be represented by a Taylor expansion:

$$\mu_a^{bleach}(F) = \mu_0^{bleach}\left(1 - \frac{F}{\beta} + \frac{F^2}{2\beta^2} - \cdots\right)$$

Thus, the general form for strong $F$ is:

$$\mu_a(F) \approx \mu_{a,0} + a_{1,a}F + a_{2,a}F^2 + \mathcal{O}(F^3).$$

The reduced scattering coefficient changes due to thermo-mechanical effects induced by the energy absorbed from the light field. The rate of change is often modeled as:

$$\frac{\partial\mu_s'}{\partial t} = \gamma\mu_a\Phi \quad \Longrightarrow \quad \mu_s'(F) = \mu_{s,0}' + \gamma\int_0^F \mu_a(F')\,dF'$$

By substituting from the series expansion of $\mu_a$ (F), The reduced scattering coefficient changes as follows:

$$\mu_s'(F) \approx \mu_{s,0}' + s_1F_1 + s_2F_2^2$$

where: $s_1 = \gamma\mu_{a,0}$, $s_2 = \gamma a_{1,a}/2$. These coefficients ($s_1$, $s_2$) represent scattering changes induced by thermal or structural damage effects. By combining both absorption and scattering effects, the total effective attenuation coefficient becomes:

$$\mu_t'(F) \approx \mu_{t,0}' + a_1F_1 + a_2F_2^2$$

here $a_1 = a_{1,a} + s_1$, $a_2 = a_{2,a} + s_2$. Using a Taylor expansion for $\delta_0 = 1/\mu_t'(F)$, to obtain:

$$\delta_{opt}(F) \approx \delta_0\left(1 - \frac{a_1}{\mu_{t,0}'}F + \frac{a_1^2 - a_2\mu_{t,0}'}{\left(\mu_{t,0}'\right)^2}F^2\right) \approx \delta_o(1 + CF + QF^2)$$

with coefficients $C = -a_1/\mu_{t,0}'$ and $Q = (a_1^2 - a_2\mu_{t,0}')/(\mu_{t,0}')^2$.This provides the nonlinear law linking dose to penetration depth, with coefficients derived from fundamental photobleaching and scattering parameters. The coefficients $a_1$ and $a_2$, which describes the linear and quadratic drift of the effective attenuation coefficient $\mu_t'(F)$, can be decomposed into contributions from distinct physical processes. This allows for a mechanistic interpretation of the nonlinear penetration depth evolution. For the bleachable component, the contribution of the drift coefficients is:

$$a_1^{bleach} = -\frac{\mu_0^{bleach}}{\beta} \quad , \quad a_2^{bleach} = +\frac{\mu_0^{bleach}}{2\beta^2}$$

Summing all contributions of photobleaching, scattering drift, and photoproduct, yields:

$$a_1 = \underbrace{-\frac{\mu_0^{bleach}}{\beta}}_{a_1^{bleach}} + \underbrace{s_1}_{a_1^{scatter}} + \underbrace{a_{1,p}}_{a_1^{prod}},$$

$$a_2 = \underbrace{-\frac{\mu_0^{bleach}}{2\beta^2}}_{a_1^{bleach}} + \underbrace{s_2}_{a_2^{scatter}} + \underbrace{a_{2,p}}_{a_1^{prod}}$$

This decomposition directly links the empirical coefficients to fundamental physical parameters, enabling quantitative interpretation of PDT dynamics.

## Appendix B: Mathematical Framework for Multiphoton, Thermal-Scattering, and FCI Models

This appendix extends the core model to incorporate multiphoton absorption, thermal-scattering coupling, and the Fluorescence Curvature Index (FCI).

At high intensities ($I > 10^8$ W/m²), absorption becomes nonlinear:

$$\mu_a(I) = \mu_{a,0} + \beta_p I^p,$$

where $p = 2,3$ for two/three-photon absorption, and $\beta_p$ is the nonlinear coefficient ($m/W^{p-1}$). The bleaching kinetics generalize to:

$$\frac{\partial C}{\partial t} = -\left(\frac{\Phi}{\beta_1} + \sigma_p I^p\right) C\,,$$

where $\Phi/\beta_1$ represents the standard first-order bleaching rate (as in Appendix A). $\sigma_p I^p$ represents the $p$-photon bleaching rate, where $\sigma_p$ is the $p$-photon bleaching cross-section. The dose is now defined in terms of time and intensity. Assuming constant intensity $I$, the dose $F = I \cdot t$. The differential equation is solved by separation of variables:

$$C(F) = C_0 \exp\left[-\left(\frac{1}{\beta_1} + \sigma_p I^{p-1}\right) F\right].$$

(since $\Phi \approx I$ in a scattering medium). This result yields an intensity-dependent effective bleaching constant $\beta_{eff} = \left(\frac{1}{\beta_1} + \sigma_p I^{p-1}\right)^{-1}$. The absorption coefficient becomes:

$$\mu_a^{bleach}(F) = \mu_0^{bleach}\left(1 - \left(\frac{1}{\beta_1} + \sigma_p I^{p-1}\right) + \frac{1}{2}\left(\frac{1}{\beta_1} + \sigma_p I^{p-1}\right)^2 F^2 - \cdots\right)$$

This introduces intensity dependence into the drift coefficienta1 $a_1$, affecting $\delta_{opt}$(F) evolution.

The reduced scattering coefficient is modeled as a function of both dose $F$ and the temperature rise $\Delta T(F)$ caused by the absorption of light:

$$\mu_s'(F, \Delta T) = \mu_{s,0}'[1 - \alpha_T \Delta T] + \gamma F$$

where $\alpha_T$ quantifies thermal scattering reduction, and $\gamma$captures damage-induced drift ($\gamma > 0$: increase;$\gamma <$ 0: clearing). For many practical cases in PDT, where heating is moderate and not the primary mechanism, a simplifying steady-state assumption can be made. Furthermore, if we neglect spatial heterogeneity and assume the heat is dissipated primarily by blood perfusion, the bioheat equation can be drastically simplified:

$$\Delta T \approx \frac{\mu_a \Phi}{\omega_b c_b}$$

Since the dose is $F = \Phi . t$, the time-integrated thermal effect becomes proportional to the total dose. For a fixed treatment time $t$, this simplifies to:$\Delta T \approx \kappa F$ , where $\kappa = \frac{\mu_a}{\omega_b c_b t}$. Substituting into the scattering model to get:

$$\mu_s'(F) \approx \mu_{s,0}' + \underbrace{\left(\gamma - \mu_{s,0}' \alpha_T \kappa\right)}_{s_1} F$$

This provides a direct physical interpretation for the linear scattering drift coefficient $s_1$ introduced in Appendix A. It is a combination of a direct damage effect ($\gamma$) and a thermally-mediated effect.

The FCI classifies regimes using normalized fluorescence:

$$\text{FCI} = \frac{d^2 f/dt^2}{df/dt}$$

If FCI > 0 (Non-inverse regime): Deceleration in fluorescence decay ($df/dt$ decreases). It indicates bleaching dominance or bulk clearing. Suggests progressive and often uniform depletion of the photosensitizer throughout the tissue volume, or increased light penetration enabling more effective bleaching in deeper layers.. In case FCI $< 0$ (Inverse regime): Acceleration in decay ($df/dt$ increases). Suggests surface-confined effects (e.g., multiphoton absorption, superficial scattering). Typically caused by phenomena such as multiphoton absorption or superficial scattering increases, which concentrate photodynamic activity near the tissue surface and lead to rapid initial fluorescence loss.

**Conflict of interest:** NIL

**Funding:** NIL

## References

[1] Songca, S.P. (2023). Combinations of Photodynamic Therapy with Other Minimally Invasive Therapeutic Technologies against Cancer and Microbial Infections. *International Journal of Molecular Sciences*, 24(13), 10875

[2] Kim, M.M. & Darafsheh, A. (2020). Light Sources and Dosimetry Techniques for Photodynamic Therapy. Photochemistry and Photobiology, 96(2), 280–294.

[3] Valentine, R.M. et al.. (2013). Modelling fluorescence in clinical photodynamic therapy. *Photochemical & Photobiological Sciences*, 12, 203–213.

[4] Shimojo, Y. et al. (2020). Measurement of absorption and reduced scattering coefficients in Asian human epidermis, dermis, and subcutaneous fat tissues in the 400–1100 nm wavelength range for optical penetration depth and energy deposition analysis. *Journal of Biomedical Optics*, 25(4), 045002

[5] Kachynski, A.V. et al. (2014). Photodynamic therapy by in situ nonlinear photon conversion. *Nature Photonics*, 8, 455–463.

[6] Pogue, B.W. et al. (2010). Fluorescent molecular imaging and dosimetry tools in photodynamic therapy. In: Gomer, C.J. (ed.), *Photodynamic Therapy, Methods in Molecular Biology* (Vol. 635). *Springer*, New York, pp. 207–227.

[7] Nielsen, K.P. et al. (2005). Choice of optimal wavelength for PDT: The significance of oxygen depletion. *Photochemistry and Photobiology*, 81, 1190–1194.

[8] Verkruysse, W. et al. (1993). Modeling the effect of wavelength on the pulsed dye laser treatment of port wine stains. *Applied Optics*, 32(4), 393–398

[9] Jonasson, H. et al. (2023). Absorption and reduced scattering coefficients in epidermis and dermis from a Swedish cohort study. *Journal of Biomedical Optics*, 28(11), 115001.

[10] Das, K. et al. (2021). Simple detection of absorption change in skin tissue using simulated spectral reflectance database. *Measurement*, 182, 109684.

[11] Izumoto, A. et al. (2019). Singlet oxygen model evaluation of interstitial photodynamic therapy with 5-aminolevulinic acid for malignant brain tumor. *Journal of Biomedical Optics*, 25(6), 063803.

[12] Panjehpour, M. et al. (1993). Comparative study between pulsed and continuous wave lasers for Photofrin photodynamic therapy. *Lasers in Surgery and Medicine*, 13(3), 296–304.

[13] Shimojo, Y. et al. (2020). Measurement of absorption and reduced scattering coefficients in Asian human epidermis, dermis, and subcutaneous fat tissues in the 400–1100 nm wavelength range for optical penetration depth and energy deposition analysis. *Journal of Biomedical Optics*, 25(4), 045002.

[14] Finlayson, L.A., McMillan, L.T., Suveges, S., Steele, D., Eftimie, R., Trucu, D., Brown, C.T.A., Eadie, E., Hossain-Ibrahim, K. and Wood, K. (2024) 'Simulating photodynamic therapy for the treatment of glioblastoma using Monte Carlo radiative transport', *Journal of Biomedical Optics*, 29(2), p. 025001.

[15] Kazempour, H. (2024) "Computational modelling of the therapeutic outputs of photodynamic therapy on spheroid-on-chip models", *Journal of Photochemistry and Photobiology B: Biology*, 258, p. 112960.

[16] Wojtkiewicz, S. & Liebert, A. (2021) "Parallel, multi-purpose Monte Carlo code for simulation of light propagation in segmented tissues", *Biocybernetics and Biomedical Engineering*, 41(4), pp. 1303–1321.

[17] Myrzakhmetov, B., Arnoux, P., Mordon, S., Acherar, S., Tsoy, I. and Frochot, C. (2021) 'Photophysical Properties of Protoporphyrin IX, Pyropheophorbide-a and Photofrin® in Different Conditions', *Pharmaceuticals*, 14(2), p. 138.

[18] (2019) 'Effect of Environment on Protoporphyrin IX: Absorbance, Fluorescence and Nonlinear Optical Properties', *Journal of Fluorescence*, 29(3), pp. 531-540.

[19] Peng, M., Mo, X., Tan, L., Tao, X., Ouyang, Y., Zhou, Y., Liang, Y., and Zhao, J. (2025) 'Ultra-high nonlinear absorption coefficients based on multiphoton-excited self-trapped excitons in perovskite-inspired copper halides', *Journal of Materials Chemistry C*, 13, pp. 3273-3282.